

## Chapter 2

# Optical Aspects of Thin Films and Interfaces

Much of the presented work has been devoted to the design of photonic structures by soft matter selfassembly. This chapter shall give a general introduction to the optics of thin films and interfaces and furthermore explain the main concepts and techniques that were used to analyse the experimental results.

### Propagation of Light at an Optical Interface: Reflection and Refraction

The propagation of electromagnetic (EM) waves in an optical medium is in the classical limit fully described by the four Maxwell equations, [1]. This leads to boundary conditions for the parallel ( $\parallel$ ) and perpendicular ( $\perp$ ) field components which need to be met when a beam of light hits a planar interface between two homogeneous lossless dielectric media with permittivity  $\epsilon_1$  and  $\epsilon_2$ , and permeability  $\mu_1$ , and  $\mu_2$ , as illustrated in Fig. 2.1a [2].

$$\epsilon_1 E_1^\perp = \epsilon_2 E_2^\perp \quad (2.1)$$

$$B_1^\perp = B_2^\perp \quad (2.2)$$

$$\mathbf{E}_1^\parallel = \mathbf{E}_2^\parallel \quad (2.3)$$

$$\mathbf{B}_1^\parallel / \mu_1 = \mathbf{B}_2^\parallel / \mu_2. \quad (2.4)$$

These four Eqs. 2.1–2.4 are the basis for the theory of reflection and refraction at optical interfaces. With a monochromatic planar incident wave of form  $E_i = E_{0,i} \exp[i(\mathbf{k}_i \mathbf{r} - \omega_i t)]$  one can derive from Eq. 2.3 the law of reflection [3]:

$$\theta_i = \theta_r = \theta_1, \quad (2.5)$$

as well as Snell's law of refraction:

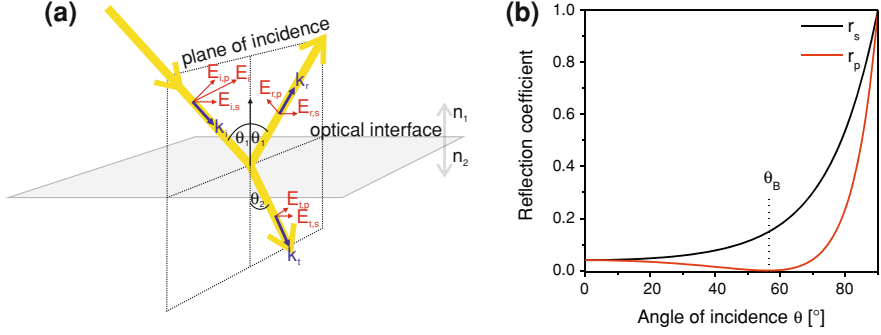


**Fig. 2.1** Reflection and refraction at an optical interface. **a** Incident ( $\mathbf{E}_i, \mathbf{k}_i$ ), reflected ( $\mathbf{E}_r, \mathbf{k}_r$ ) and refracted ( $\mathbf{E}_t, \mathbf{k}_t$ ) EM waves at the interface between two homogeneous, isotropic and lossless dielectric media. The electric field can be decomposed into parallel ( $\mathbf{E}_p$ ) and perpendicular ( $\mathbf{E}_s$ ) components with respect to the plane of incidence. **b** Reflection coefficients at an air-glass interface for parallel ( $r_p$ ) and perpendicular ( $r_s$ ) polarised incident light as a function of angle of incidence ( $\theta$ ). At the Brewster angle  $\theta_B = 56.5^\circ$  all parallel polarised light is refracted ( $r_p = 0$ ), i.e. the reflected light is fully polarised perpendicularly to the plane of incidence

$$n_1 \sin \theta_1 = n_2 \sin \theta_2. \quad (2.6)$$

The relative amplitudes of incident, reflected and refracted waves depend on their polarisation with respect to the plane of incidence. Incoming light can be decomposed into orthogonal and linearly polarised waves, with  $\mathbf{E}$ -field components perpendicular ( $\mathbf{E}_s$ ) and parallel ( $\mathbf{E}_p$ ) to the plane of incidence. Based on Eqs. 2.3 and 2.4 the so-called Fresnel coefficients can be derived:

$$r_s = \frac{E_{r,s}}{E_{i,s}} = \frac{n_1 \cos \theta_1 - n_2 \cos \theta_2}{n_1 \cos \theta_1 + n_2 \cos \theta_2}, \quad (2.7)$$

$$t_s = \frac{E_{t,s}}{E_{i,s}} = \frac{2n_1 \cos \theta_1}{n_1 \cos \theta_1 + n_2 \cos \theta_2}, \quad (2.8)$$

$$r_p = \frac{E_{r,p}}{E_{i,p}} = \frac{n_2 \cos \theta_1 - n_1 \cos \theta_2}{n_2 \cos \theta_1 + n_1 \cos \theta_2}, \quad (2.9)$$

$$t_p = \frac{E_{t,p}}{E_{i,p}} = \frac{2n_1 \cos \theta_1}{n_2 \cos \theta_1 + n_1 \cos \theta_2}. \quad (2.10)$$

Figure 2.1b shows the corresponding reflectance  $\mathcal{R}$  and refraction, i.e. transmittance  $\mathcal{T}$ , at a air-glass interface with  $\mathcal{R}_{s,p} = |r_{s,p}|^2$  and  $\mathcal{T}_{s,p} = (n_2 \cos \theta_2 / n_1 \cos \theta_1) \cdot |t_{s,p}|^2$ , respectively. The Brewster angle  $\theta_B$  follows from  $r_p = 0$  and Snell's law with  $\theta_B = \arctan(n_2/n_1)$ .

## Thin Film Interference

The characteristic reflection of a thin film is the consequence of multiple beam interference. As shown in Fig. 2.2a, the presence of two optical interfaces, each with its characteristic Fresnel coefficients for reflection and transmission, leads to a division of the incident beam into a multitude of coherent waves. If the reflection coefficients are non-negligible, this results in a number of higher order reflected waves that all contribute to the colour appearance of the film, which is a characteristic of its thickness ( $h_{\text{film}}$ ) and refractive index ( $n_1$ ). The optical path difference  $\Delta$  of two adjacent rays is given by:

$$\Delta = 2n_1 h_{\text{film}} \cos \theta_1, \quad (2.11)$$

with a corresponding phase shift  $\phi_m = (m + 1) \cdot (2\pi/\lambda) \cdot \Delta$ , where  $m$  is the number of total internal reflections.  $\mathbf{E}_1$  is therefore out-of-phase by  $180^\circ$  compared to all higher order reflected waves ( $\mathbf{E}_2, \mathbf{E}_3, \dots$ ), where  $m$  is always an odd number. The resulting overall amplitude is then given by a geometric series, where  $r_{ij}$  and  $t_{ij}$  correspond to the Fresnel coefficients at the optical interface  $i$  and  $j$  denoted in order of the propagation direction of the ray [4]. This applies for perpendicular polarisation (with  $r_{s,ij}$  and  $t_{s,ij}$ ) and parallel polarisation (with  $r_{p,ij}$  and  $t_{p,ij}$ ).

$$\begin{aligned} \frac{E_r}{E_0} &= r_{01} + t_{01}r_{12}t_{10} \exp^{-2i\phi} \sum_{n=1}^{\infty} (-1)^n (r_{12}r_{10})^n \exp^{-2in\phi} \\ &= r_{01} + \frac{t_{01}r_{12}t_{10} \exp^{-2i\phi}}{1 + r_{10}r_{12} \exp^{-2i\phi}} = \frac{r_{01} + r_{12} \exp^{-2i\phi}}{1 + r_{10}r_{12} \exp^{-2i\phi}}, \end{aligned} \quad (2.12)$$

with  $t_{01}t_{10} = \sqrt{1 - r_{01}^2} \sqrt{1 - r_{10}^2} = 1 - r_{01}^2$ , assuming lossless dielectric media. The reflectivity of a thin film is then given by

$$\begin{aligned} \mathcal{R} &= \frac{I_r}{I_0} = \frac{(r_{01} + r_{12} \exp^{-2i\phi})(r_{01} + r_{12} \exp^{2i\phi})}{(1 + r_{01}r_{12} \exp^{-2i\phi})(1 + r_{01}r_{12} \exp^{2i\phi})} \\ &= \frac{r_{01}^2 + r_{12}^2 + 2r_{01}r_{12} \cos 2\phi}{1 + r_{01}^2 r_{12}^2 + 2r_{01}r_{12} \cos 2\phi}. \end{aligned} \quad (2.13)$$

For illustration, a computer-simulated colour reflection of a thin water film is shown in Fig. 2.2. According to Eq. 2.11, the conditions for multiple beam interference depend on the film thickness ( $h$ ) and the angle of inclination ( $\theta$ ), here plotted in polar coordinates.

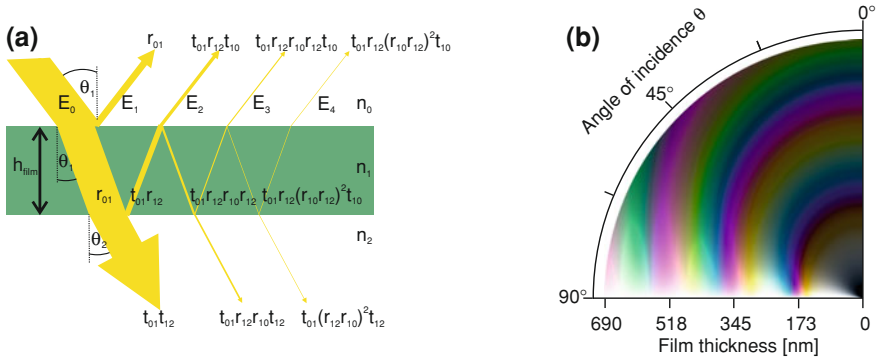


**Fig. 2.2** Thin film interference. **a** The Fresnel equations determine the reflection and transmission coefficients of EM waves at each optical interface. The overall reflectivity of a thin film is therefore a superposition of a multitude of beams with different optical paths. **b** Computer-simulation illustrating the colour reflection of a thin water film plotted in polar coordinates as a function of the film thickness ( $r$ ) and the angle of incidence ( $\theta$ ) for unpolarised standard daylight illumination (D65). **b** Adapted with permission from [5]

## Model of Multilayer Reflectivity

### *Rouard's Method*

The optical response of a multilayer stack, i.e. a layer sequence of thin films, results from the reflection and refraction characteristics at each of its optical interfaces. In analogue to the mathematical treatment for thin film interference, Rouard extended the method of summation in a stepwise procedure from one layer with two interfaces to  $k$  layers and  $k + 1$  interfaces [4, 6]. Following his technique, the optical properties of the  $k$ -th individual layer (in terms of reflection coefficient and accompanying phase change) at the bottom of the stack are replaced by a single surface with the appropriate characteristics. This is then incorporated into the calculation for the adjacent  $(k - 1)$ th layer and so on. Based on Eq. 2.12 it follows for the amplitude  $\rho_k$  and phase  $\delta_k$  of the light reflected from the  $k$ th layer:

$$\rho_k \exp^{i\delta_k} = \frac{r_k + r_{k+1} \exp^{-2i\phi_k}}{1 + r_k r_{k+1} \exp^{-2i\phi_k}}. \quad (2.14)$$

The  $k$ th layer is subsequently treated as a surface with the effective Fresnel coefficient  $\rho_k \exp^{i\delta_k}$ . The parameter  $\rho_k$  can be calculated via the complex conjugate

$$\rho_k^2 = \frac{r_k^2 + r_{k+1}^2 + 2r_k r_{k+1} \cos 2\phi_k}{1 + r_k^2 r_{k+1}^2 + 2r_k r_{k+1} \cos 2\phi_k}. \quad (2.15)$$

$\delta_k$  can be written as [4]

$$\delta_k = \eta_k - \xi_k, \quad (2.16)$$

with

$$\tan \xi_k = \frac{r_{k+1} \sin 2\phi_k}{r_k + r_{k+1} \cos 2\phi_k} \quad (2.17)$$

and

$$\tan \eta_k = \frac{r_k r_{k+1} \sin 2\phi_k}{1 + r_k r_{k+1} \cos 2\phi_k}. \quad (2.18)$$

For the adjacent  $(k - 1)$ th layer this results in

$$\rho_{k-1} \exp^{i\delta_{k-1}} = \frac{r_{k-1} + \rho_k \exp^{-i\delta_k} \exp^{-2i\phi_{k-1}}}{1 + r_{k-1} \rho_k \exp^{-i\delta_k} \exp^{-2i\phi_{k-1}}}, \quad (2.19)$$

where  $\rho_{k-1}$  and  $\delta_{k-1}$  can be calculated accordingly following Eqs. 2.15–2.18. This process is repeated  $k$ -times to obtain the reflection coefficient of the overall system  $\rho_1$ .

### *Transfer Matrix Method*

An alternative route to calculate the optical response of a multilayer stack is the so-called transfer matrix approach, which relates the electric and magnetic field at both interfaces of an optical element via a characteristic matrix [7, 8]. Assume an incoming beam at normal incidence and a single layer of optical thickness  $l$  in-between two optical media, i.e. a sequence media 0-layer 1-media 2. The boundary conditions, introduced in Eqs. 2.1–2.4, have to be fulfilled at interface 01:

$$E_{0i} + E_{0r} = E_{1i} + E_{1r} \quad (2.20)$$

$$n_0 E_{0i} - n_0 E_{0r} = n_1 E_{1i} n_1 E_{1r}, \quad (2.21)$$

and at interface 12:

$$E_{1i} \exp^{ikl} + E_{1r} \exp^{-ikl} = E_t \quad (2.22)$$

$$n_1 E_{1i} \exp^{ikl} - n_1 E_{1r} \exp^{-ikl} = n_2 E_t. \quad (2.23)$$

This set of equations can be combined to

$$1 + \frac{E_{0r}}{E_{0i}} = \left( \cos kl - i \frac{n_2}{n_1} \sin kl \right) \frac{E_t}{E_{0i}} \quad (2.24)$$

$$n_0 - n_o \frac{E_{0r}}{E_{0i}} = \left( -in_1 \sin kl + n_2 \cos kl \right) \frac{E_t}{E_{0i}}, \quad (2.25)$$

or equivalently in a matrix representation

$$\begin{pmatrix} 1 \\ n_0 \end{pmatrix} + \begin{pmatrix} 1 \\ -n_0 \end{pmatrix} \frac{E_{0r}}{E_{0i}} = \begin{pmatrix} \cos kl & (-i/n_1) \sin kl \\ -in_1 \sin kl & \cos kl \end{pmatrix} \begin{pmatrix} 1 \\ n_2 \end{pmatrix} \frac{E_t}{E_{0i}}. \quad (2.26)$$

For clarity, Eq. 2.26 can be written as

$$\begin{pmatrix} 1 \\ n_0 \end{pmatrix} + \begin{pmatrix} 1 \\ -n_0 \end{pmatrix} r = M \begin{pmatrix} 1 \\ n_2 \end{pmatrix} t, \quad (2.27)$$

where  $r$  is the reflection coefficient,  $t$  is the transmission coefficient and  $M$  is the transfer matrix. The extension to the optical response of  $N$ -layers is then accordingly

$$\begin{pmatrix} 1 \\ n_0 \end{pmatrix} + \begin{pmatrix} 1 \\ -n_0 \end{pmatrix} r = M_1 M_2 M_3 \dots M_N \begin{pmatrix} 1 \\ n_2 \end{pmatrix} t = M_{\text{tot}} \begin{pmatrix} 1 \\ n_2 \end{pmatrix} t, \quad (2.28)$$

where  $M_{\text{tot}}$  is the product of the individual transfer matrices.

A multilayer stack of particular interest is a distributed Bragg reflector (DBR), which consists of an periodic sequence of high and low refractive index layers. Strong reflection arises when all reflected beams are of equal phase and therefore interfere constructively at the front surface. This is fulfilled for  $n_{\text{low}} h_{\text{low}} = n_{\text{high}} h_{\text{high}} = \lambda/4$ . DBRs are therefore typically denoted as quarter-wave stacks [9]. The product of two adjacent transfer matrices is

$$\begin{pmatrix} 0 & -i/n_{\text{low}} \\ -in_{\text{low}} & 0 \end{pmatrix} \begin{pmatrix} 0 & -i/n_{\text{high}} \\ -in_{\text{high}} & 0 \end{pmatrix} = \begin{pmatrix} n_{\text{high}}/n_{\text{low}} & 0 \\ 0 & -n_{\text{low}}/n_{\text{high}} \end{pmatrix}, \quad (2.29)$$

and correspondingly for the overall optical element with  $2N$  layers

$$M = \begin{pmatrix} n_{\text{high}}/n_{\text{low}} & 0 \\ 0 & -n_{\text{low}}/n_{\text{high}} \end{pmatrix}^N = \begin{pmatrix} (n_{\text{high}}/n_{\text{low}})^N & 0 \\ 0 & (-n_{\text{low}}/n_{\text{high}})^N \end{pmatrix}. \quad (2.30)$$

The reflectance of the multilayer stack can then be obtained by solving Eq. 2.27 for  $r$

$$\mathcal{R} = |r|^2 = \left[ \frac{(n_{\text{high}}/n_{\text{low}})^{2N} - 1}{(n_{\text{high}}/n_{\text{low}})^{2N} + 1} \right]^2 \quad (2.31)$$

The position of the reflectance maximum can be calculated by geometric considerations [10]:

$$m\lambda_{\text{max}} = 2 \left( h_1 \sqrt{n_1^2 - n_0^2 \sin^2 \theta_i} + h_2 \sqrt{n_2^2 - n_0^2 \sin^2 \theta_i} \right), \quad (2.32)$$

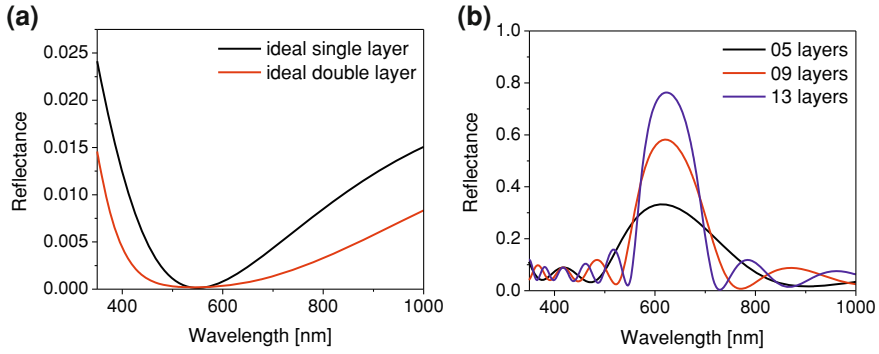


**Fig. 2.3** Modelling of multilayer interference. **a** Calculated reflectance at normal incidence for interference-based antireflective coatings (ARC) optimised for  $\lambda = 550$  nm. An ideal single layer ARC yields  $n_{\text{ARC}} = 1.22$  and  $h_{\text{ARC}} = 112$  nm to fulfill the amplitude and phase matching conditions on a glass substrate ( $n_{\text{subs}} = 1.50$ ). The ideal double layer configuration is calculated for comparison, with  $n_{\text{ARC}_{\text{low}}} = 1.11$ ,  $h_{\text{ARC}_{\text{low}}} = 123$  nm,  $n_{\text{ARC}_{\text{high}}} = 1.36$  and  $h_{\text{ARC}_{\text{high}}} = 101$  nm. **b** Reflectance at normal incidence for multilayer stacks consisting of an odd number of alternating  $\lambda/4$  layers of high and low refractive index on a glass substrate, with  $n_{\text{high}} = 1.69$ ,  $h_{\text{low}} = 75$  nm,  $n_{\text{low}} = 1.41$ ,  $h_{\text{high}} = 130$  nm and  $n_{\text{subs}} = 1.50$

where  $h_{1,2}$  and  $n_{1,2}$  are the layer thickness and refractive index of component 1 and 2, respectively and  $m \in \mathbb{N}$ .

To model multilayer structures in this work, Rouard's technique was implemented into a "MatLab" algorithm that was developed by Dr. Mathias Kolle [10]. An alternative method based on a transfer matrix algorithm was used for comparison [11]. The optical constants of the building blocks were determined individually by spectroscopic ellipsometry. Figure 2.3a shows example calculations for interference-based antireflective coatings (ARC) which consist of one or two layers on a glass substrate to allow for amplitude and phase matching [12]. Wavelength-dependent optical constants were used to account for the optical dispersion of the used materials. In Fig. 2.3b an optical model is presented for stacks of  $\lambda/4$  layers with alternating high and low refractive index layers on a glass substrate. An odd number of overall layers corresponds to the high refractive index layer being adjacent to the air-stack and stack-substrate interfaces.

## From Periodic Multilayer Stacks to Photonic Crystals

The model calculation presented in Fig. 2.3b illustrates the change in optical response when extending the number of building blocks of a DBR. A further increase in the refractive index contrast or number of layers ultimately leads to sharply defined, frequency-dependent reflection and transmission characteristics. The alternating sequence of high and low refractive index layers represents a dielectric lattice and can therefore be regarded as a one-dimensional (1D) photonic crystal. Similar to

electron propagation in atomic crystals, the periodic modulation of the dielectric creates a potential landscape which determines the propagation directions of photons within the material as a function of frequency. In the case of high symmetries and dielectric contrast, a full three-dimensional photonic band gap can develop for a defined frequency range. This concept was first introduced by Yablonovitch [13] and John [14] and has become a very active field of research ever since [15, 16].

The main function, that contains all the information for a given dielectric system is the magnetic vector field  $\mathbf{H}(\mathbf{r}, t) = \mathbf{H}(\mathbf{r})e^{i\omega t}$ . Based on the fact that macroscopic electromagnetism is governed by the four Maxwell equations, a so-called master equation can be deduced:

$$\nabla \times \left( \frac{1}{\varepsilon(\mathbf{r})} \nabla \times \mathbf{H}(\mathbf{r}) \right) = \frac{\omega^2}{c^2} \mathbf{H}(\mathbf{r}), \quad (2.33)$$

which is the analogon to the Schrödinger equation for the quantum mechanical consideration of an electron. See reference [17] for a comprehensive derivation.

The periodicity of the system is given by the permittivity  $\varepsilon(\mathbf{r}) = \varepsilon(\mathbf{r} + \mathbf{R})$  for all lattice vectors  $\mathbf{R}$ . It is essential that  $\nabla \mathbf{H} = 0$ , i.e. the vector field has to be source- and sink-free as well as transverse. Assuming that the Maxwell operator  $\hat{\Theta} = \nabla \times (\varepsilon(\mathbf{r})^{-1} \nabla \times)$  is a linear Hermitian operator, one can use a variational theorem to determine the normal modes and frequencies:

$$E_{\text{var}} = \frac{(\mathbf{H}, \hat{\Theta} \mathbf{H})}{(\mathbf{H}, \mathbf{H})} \quad (2.34)$$

The band structure functions  $\omega_n(\mathbf{k})$  of a photonic crystal can therefore be exactly calculated *ab initio* from  $\varepsilon(\mathbf{r})$  by applying a computational scheme to solve the master equation for the magnetic modes of the photonic crystal under the given boundary conditions. Typical approaches are the finite difference time domain method [20] or the planar wave expansion method [21], which is presented for a 1D model system in reference [10]. Accordingly, the bandwidth of the fundamental reflection peak  $\Delta\lambda_{\text{max}}$  (full width at half max) for a photonic crystal-like DBR can be calculated [17] with

$$\Delta\lambda_{\text{max}} = \frac{4\lambda_{\text{max}}}{\pi} \sin^{-1} \left( \frac{n_{\text{high}} - n_{\text{low}}}{n_{\text{high}} + n_{\text{low}}} \right). \quad (2.35)$$

## Optical Properties of Porous Thin Films

In many different aspects, this work explores structure control in mesoporous materials on the 10 nm length scale. Conceptually, block copolymer (BCP) self-assembly offers precise control over the pore architecture, pore size and pore volume (i.e. porosity) in thin dielectric films. The optical properties of mesoporous materials are not simply a consequence of the constituent materials' crystal band structures, but



are dependent on pore dimensions and volume on sub-optical length scales. While generally the real and imaginary parts of the refractive index are an intrinsic property of the material, these can be finely tuned by adjusting the porosity as well as infiltration and blending of the mesostructure with other materials.

Metamaterials are a particular example where morphological arrangement on the sub-wavelength scale is of central importance for the resulting optical properties [20, 21]. The experimental realisation of a material with negative refractive index  $n = \sqrt{\mu\varepsilon} < 0$  typically requires negative permeability  $\mu$  and permittivity  $\varepsilon$  in the same frequency range. This can be realised by a so-called split-ring resonator geometry, experimentally achieved for microwave to infrared frequencies [22–24]. Currently, access to visible frequencies is impeded by resolution limits in the fabrication process. Alternative approaches have been developed but their experimental realisation remains a major challenge [25]. An alternative concept is a chiral route to negative refraction [26]. In a chiral medium the refractive index is polarisation-dependent. The band splitting of the resonant transverse modes leads to a range of frequencies, where the group velocity  $v_g = \partial\omega/\partial k$  has an opposite sign to the phase velocity  $v_p = \omega/k$ , leading to  $n < 0$  for a certain polarisation. The validity of this concept has already been shown at terahertz frequencies [27]. However, like for other metamaterial concepts such as split-ring resonators, it proves difficult to scale down the structural feature sizes to achieve negative refraction in the visible spectral range.

As outlined in “[Structure Formation in Block Copolymer Systems](#)” the self-assembly of BCP systems allows access to well defined nanoarchitectures. BCP morphologies have unit-cells far smaller than the wavelength of light, which makes this system an interesting platform for the bottom-up assembly of optical metamaterials. A possible materials route to BCP-templated arrays is illustrated in Fig. 2.4, where the metal structure is fabricated in four steps: (1) BCP self-assembly in a thin film, (2) selective etching of one of the polymer blocks, (3) backfilling of the template with a metal, such as silver or gold and (4) selective etching of the residual polymer components [28]. Of particular relevance to optical applications are bicontinuous gyroid morphologies. For a diblock copolymer, the double gyroid consists of two network structures of block A separated by a complementary matrix of block B (Fig. 2.4a) [29]. This is the equilibrium arrangement if one of the polymer blocks exhibits a volume fraction of 33–37 % [30]. When extending from an diblock copolymer, with segments A and B, to a three component system, with blocks A, B and C, the compositional window for the symmetric double gyroid morphology is significantly larger in a ternary phase diagram where the blocks arrange in an ABCBA core-shell structure (Figure 2.4b, space group:  $la\bar{3}d$  ( $Q^{230}$ )). Additionally, a three component system allows access to a chiral phase morphology (Figure 2.4c, space group:  $I4_132$  ( $Q^{214}$ )) [31, 32].

In fact, linear dichroism and gyrotropic light propagation has been experimentally shown for a chiral alternating gyroid structure made of gold, analogue to Fig. 2.4c [33]. Theoretical models predict a negative refractive index in the visible and near-infrared range for a symmetric double gyroid morphology after infiltration with silver or aluminium [28].

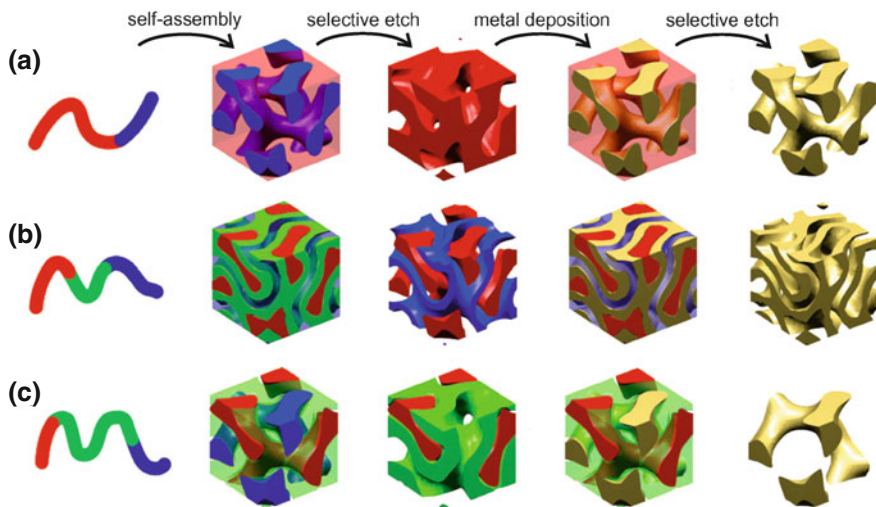


**Fig. 2.4** BCP route to metamaterials at visible frequencies. The templating approach involves four processing steps: (1) BCP self-assembly in a thin film, (2) selective etching of one of the polymer blocks, (3) backfilling of the template with a metal and (4) selective removal of the residual polymer components. The resulting network symmetry depends on the employed BCP: **a** Diblock copolymer yielding a double gyroid morphology. **b** Triblock copolymer resulting in a double gyroid morphology. **c** Triblock terpolymer route to an alternating gyroid, a chiral morphology. **a–c** Adapted with permission from [28]. Copyright 2011 Wiley

In lossless dielectric films, the effect of morphology on the optical response is much less pronounced. For model systems with spherical pores in a symmetric arrangement as illustrated in Fig. 2.5a, the pore size and spatial periodicity (SC, BCC, FCC) have no effect on the resulting optical properties. These are simply determined by the pore volume for pore diameters  $d_{\text{iam}} \gg \lambda$  and sufficiently thick films  $h_{\text{film}}/d_{\text{iam}} \geq 150$  [34]. Nevertheless, the spatial arrangement of material will have an influence on how porosity can be controlled and adjusted. The conventional sintering of nanoparticles to form mesoporous films only allows a variation of porosity between  $\approx 30\text{--}40\%$  [35]. This is due to the fact that porosity is generated by the random close packing of nanoparticles, which somewhat limits the control over pore size and pore volume [36]. By blending with additional sacrificial material, porosity can be increased up to  $60\%$  [37]. In contrast, the use of BCPs as templates or structure directing agents for the assembly of inorganic films offers a much higher control over pore size and porosity, even if the film morphology may not be of particular importance. This aspect is further explored in Chap. 5.

Mesoporous materials exhibit pores of  $5\text{--}50\text{ nm}$  length scale, too small to be resolved using visible light. As a consequence, the compositional arrangement can be treated as an effective medium, with optical constants that depend on the volume fractions of the constituents. There are a number of different physical models that relate the macroscopic properties of a medium to the relative volume fraction of its

components. The most intuitive approach has been established by Birchak et al., which describes the effective index of the medium by the linear combination of its volume fractions, i.e.

$$n_{\text{eff}} = (1 - f_p)n_m + f_p n_p, \quad (2.36)$$

where  $f_p$  is the volume fraction of the pores, and  $n_m$  and  $n_p$  are the refractive indices of the matrix and pore forming material, respectively [38].

A physical model for the relation between the dielectric constant of an lossless optical medium and the polarisability of its constituent molecules has been introduced by Mossotti and Clausius [39, 40].

$$\frac{n_{\text{eff}}^2 - 1}{n_{\text{eff}}^2 + 2} = \frac{4\pi}{3}\alpha q, \quad (2.37)$$

where  $n_{\text{eff}}$  is the effective refractive index of the overall medium,  $\alpha$  is the molecular polarisability and  $q$  is the number of molecules per unit volume. Their analytic solution is based on a dielectric medium which is built up of polarisable objects in empty space in a perfectly mixed, homogeneous and isotropic configuration [41]. When  $\alpha$  is modified to account for the local field of nearby atoms, the Clausius-Mossotti model is also valid for homogeneous solid state materials [42].

The extension of the Clausius-Mossotti equation to a mixture of constituents and volume fractions was developed by Lorenz and Lorenz [43, 44].

$$\frac{n_{\text{eff}}^2 - 1}{n_{\text{eff}}^2 + 2} = f_1 \left( \frac{n_1^2 - 1}{n_1^2 + 2} \right) + f_2 \left( \frac{n_2^2 - 1}{n_2^2 + 2} \right), \quad (2.38)$$

where  $n_1$  and  $n_2$  are the refractive indices of component 1 and 2 and  $f_1$  and  $f_2$  are their volume fractions [45]. The Clausius-Mossotti-Lorenz-Lorenz model assumes mixing of polarisable objects on the molecular level. It does not take into account that the constituents may form domains that are large enough to exhibit their own dielectric identity.

The Maxwell-Garnett model considers mesoscopic domains by shifting from a vacuum lattice with polarisable point objects to a host-guest approach for the dielectric components. The minority component ( $n_p$ ,  $f_p$ ) then forms inclusions, i.e. pores, in a host matrix that is formed by the majority component ( $n_m$ ).

$$\frac{n_{\text{eff}}^2 - n_m^2}{n_{\text{eff}}^2 + 2n_m^2} = f_p \frac{n_p^2 - n_m^2}{n_p^2 + 2n_m^2}. \quad (2.39)$$

The host-guest model assumes  $f_m \gg f_p$  and  $n_m > n_p$ . In cases where the volume fraction of pores becomes comparable or predominant, this approach may not be valid. A more general expression is

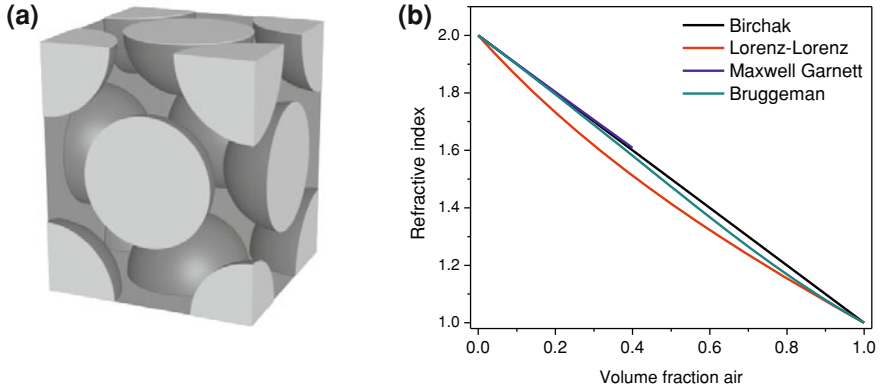


**Fig. 2.5** Effective medium approximation. **a** Schematic of a two component film with close-packed pores. **b** Refractive index versus porosity for different effective medium approximations with  $n_{\text{high}}=2$ . The Maxwell-Garnett model assumes one majority component and  $n_m > n_p$ , which is only valid in a limited range. **a** Adapted with permission from [46]. Copyright Mathias Kolle

$$\frac{n_{\text{eff}}^2 - n_h^2}{n_{\text{eff}}^2 + 2n_h^2} = f_a \frac{n_a^2 - n_h^2}{n_a^2 + 2n_h^2} + f_b \frac{n_b^2 - n_h^2}{n_b^2 + 2n_h^2}, \quad (2.40)$$

where  $n_h^2$ ,  $n_a^2$  and  $n_b^2$  are the refractive indices of the host and components a and b, respectively. This is equivalent to the Clausius-Mossotti-Lorenz-Lorenz equation for  $n_h^2 = 1$ . The expression leads to the Maxwell-Garnett model for  $n_h^2 = n_{\text{eff}}^2$ . For a self-consistent approach with  $n_h^2 = n_{\text{eff}}^2$  Eq. 2.40 reduces to

$$(1 - f_b) \frac{n_a^2 - n_{\text{eff}}^2}{n_a^2 + 2n_{\text{eff}}^2} + f_b \frac{n_b^2 - n_{\text{eff}}^2}{n_b^2 + 2n_{\text{eff}}^2} = 0. \quad (2.41)$$

This is the so-called Bruggeman effective medium approximation. The predictions of the four models are exemplified in Fig. 2.5b for an porous material with  $n_m = 2$  in air ( $n_p = 1$ ). For  $f_{p, \text{air}} = 0.3$  the deviation between Bruggeman ( $n_{\text{eff}} = 1.69$ ), Birchak ( $n_{\text{eff}} = 1.70$ ) and Maxwell-Garnett ( $n_{\text{eff}} = 1.71$ ) is well within the experimental uncertainty. In contrast, the deviation becomes significant for highly porous materials.

## References

1. J. Maxwell, A dynamical theory of the electromagnetic field. Philos. Trans. R. Soc. Lond. **155**, 459–512 (1865)
2. D. Griffiths, *Introduction to Electrodynamics*, 3rd edn. (Benjamin Cummings, New York, 1999)
3. E. Hecht, *Optics*, 4th edn. (Pearson, NJ, 2003)
4. O. Heavens, *The Optical Properties of Thin Solid Films* (Dover, New York, 1992)

5. Wikimedia-public domain graphic <http://commons.wikimedia.org> (2011)
6. P. Rouard, Etudes des propriétés optiques des lames métalliques très minces. *Annales de Physique* **7**, 291–384 (1937)
7. G. Fowles, *Introduction to Modern Optics*, 1st edn. (Dover Publications, New York, 1990)
8. M. Born, E. Wolf *Principles of Optics*, 7th edn. (Cambridge University Press, Cambridge, 1999)
9. E. Schubert, *Light-Emitting Diodes*, 2nd edn. (Cambridge University Press, Cambridge, 2006)
10. M. Kolle, Photonic structures inspired by nature. Ph.D. thesis, University of Cambridge, Physics Department, 2010
11. G. Burkhard, E. Hoke, M. McGehee, Accounting for interference, scattering, and electrode absorption to make accurate internal quantum efficiency measurements in organic and other thin solar cells. *Adv. Mater.* **22**(30), 3293–3297 (2010)
12. H. Macleod, *Thin Film Optical Filters*, 3rd edn. (Institute of Physics Publishing, Bristol, 2001)
13. E. Yablonovitch, Inhibited spontaneous emission in solid-state physics and electronics. *Phys. Rev. Lett.* **58**(20), 2059–2062 (1987)
14. S. John, Strong localization of photons in certain disordered dielectric superlattices. *Phys. Rev. Lett.* **58**(23), 2486–2489 (1987)
15. C. Lopez, Materials aspects of photonic crystals. *Adv. Mater.* **15**(20), 1679–1704 (2003)
16. K. Arpin, A. Mihi, H. Johnson, A. Baca, J. Rogers, J. Lewis, P. Braun, Multidimensional architectures for functional optical devices. *Adv. Mater.* **22**(10) SI, 1084–1101 (2010)
17. J.D. Joannopoulos, S.G. Johnson, J.N. Winn, R.D. Meade, *Photonic Crystals: Molding the Flow of Light*, 2nd edn. (Princeton University Press, Princeton, 2008)
18. A. Taflov, *Computational Electrodynamics, the Finite-Difference Time-Domain Method*, 3rd edn. (Artech House Publishers, Boston, 2005)
19. K. Ho, C. Chan, C. Soukoulis, Existence of a photonic gap in periodic dielectric structures. *Phys. Rev. Lett.* **65**(25), 3152–3155 (1990)
20. V. Veselago, Electrodynamics of substances with simultaneously negative electrical and magnetic permeabilities. *Soviet Physics Uspekhi-USSR* **10**(4), 507–514 (1968)
21. J. Pendry, Negative refraction makes a perfect lens. *Phys. Rev. Lett.* **85**(18), 3966–3969 (2000)
22. R. Shelby, D. Smith, S. Schultz, Experimental verification of a negative index of refraction. *Science* **292**(5514), 77–79 (2001)
23. V. Shalaev, W. Cai, U. Chettiar, H. Yuan, A. Sarychev, V. Drachev, A. Kildishev, Negative index of refraction in optical metamaterials. *Opt. Lett.* **30**(24), 3356–3358 (2005)
24. G. Dolling, M. Wegener, C. Soukoulis, S. Linden, Negative-index metamaterial at 780 nm wavelength. *Opt. Lett.* **32**(1), 53–55 (2007)
25. S. Burgos, R. de Waele, A. Polman, H. Atwater, A single-layer wide-angle negative-index metamaterial at visible frequencies. *Nat. Mater.* **9**(5), 407–412 (2010)
26. J. Pendry, A chiral route to negative refraction. *Science* **306**(5700), 1353–1355 (2004)
27. S. Zhang, Y.-S. Park, J. Li, X. Lu, W. Zhang, X. Zhang, Negative refractive index in chiral metamaterials. *Phys. Rev. Lett.* **102**(2), 023901 (2009)
28. K. Hur, Y. Francescato, V. Giannini, S. Maier, R. Hennig, U. Wiesner, Three-dimensionally isotropic negative refractive index materials from block copolymer self-assembled chiral gyroid networks. *Angewandte Chemie - Int. Ed.* **123**(50), 12191–12195 (2011)
29. D. Haduk, P. Harper, S. Gruner, C. Honeker, G. Kim, E. Thomas, L. Fetters, The gyroid-a new equilibrium morphology in weakly segregated diblock copolymers. *Macromolecules* **27**(15), 4063–4075 (1994)
30. C. Park, J. Yoon, E. Thomas, Enabling nanotechnology with self assembled block copolymer patterns. *Polymer* **44**(22), 6725–6760 (2003)
31. T. Epps, E. Cochran, T. Bailey, R. Waletzko, C. Hardy, F. Bates, Ordered network phases in linear poly (isoprene-b-styrene-b-ethylene oxide) triblock copolymers. *Macromolecules* **37**, 8325–8341 (2004)
32. Y. Mogi, M. Nomura, H. Kotsuji, K. Ohnishi, Y. Matsushita, I. Noda, Superlattice structures in morphologies of the ABC triblock copolymers. *Macromolecules* **27**(23), 6755–6760 (1994)

33. S. Vignolini, N.A. Yufa, P.S. Cunha, S. Guldin, I. Rushkin, M. Stefik, K. Hur, U. Wiesner, J.J. Baumberg, U. Steiner, A 3D optical metamaterial made by self-assembly. *Adv. Mater.* **24**(10), OP23-OP27 (2012)
34. N. Hutchinson, T. Coquil, A. Navid, L. Pilon, Effective optical properties of highly ordered mesoporous thin films. *Thin Solid Films* **518**(8), 2141–2146 (2010)
35. M. Calvo, S. Colodrero, N. Hidalgo, G. Lozano, C. Lopez-Lopez, O. Sanchez-Sobrado, H. Míguez, Porous one dimensional photonic crystals: novel multifunctional materials for environmental and energy applications. *Energy Environ. Sci.* **4**, 4800–4812 (2011)
36. S. Burnside, V. Shklover, C. Barbé, P. Comte, F. Arendse, K. Brooks, M. Grätzel, Self-organization of TiO<sub>2</sub> nanoparticles in thin films. *Chem. Mater.* **10**(9), 2419–2425 (1998)
37. C. Lopez-Lopez, S. Colodrero, S. Raga, H. Lindstrom, F. Fabregat-Santiago, J. Bisquert, H. Míguez, Enhanced diffusion through porous nanoparticle optical multilayers. *J. Mater. Chem.* **22**(5), 1751–1757 (2012)
38. J. Birchak, C. Gardner, J. Hipp, J. Victor, High dielectric-constant microwave probes for sensing soil-moisture. *Proc. IEEE* **62**(1), 93–98 (1974)
39. O. Mossotti, *Memorie Di Matematica E Di Fisica Della Societa Italiana Delle Scienze Residente In Modena. Nella Tipografia Camerale Modena* (1850)
40. R. Clausius, *Die mechanische Behandlung der Elektrizität* (1879)
41. P. Van Rysselberghe, Remarks concerning the Clausius-Mossotti law. *J. Phys. Chem.* **36**(4), 1152–1155 (1932)
42. R. Feynman, R. Leighton, M. Sands, *Feynman Lectures on Physics*, vol. 2, Chap. 32 (Addison Wesley, Reading, 1989)
43. L. Lorenz, Über die Refraktionsconstante. *Annalen der Physik* **11**, 70–103 (1880)
44. H. Lorenz, Über die Beziehung zwischen der Fortpflanzungsgeschwindigkeit des Lichtes der Körperdichte. *Annalen der Physik* **9**, 641–665 (1880)
45. D. Aspnes, Optical-properties of thin-films. *Thin Solid Films* **89**(3), 249–262 (1982)
46. M. Kolle, personal graphics collection

Inorganic Nanoarchitectures by Organic Self-Assembly

Guldin, S.

2013, XVII, 165 p., Hardcover

ISBN: 978-3-319-00311-5